1 **Unexpected enhancement of new particle formation by lactic acid**

2 **sulfate resulting from SO$_3$ loss in forested and agricultural regions**

3 **Rui Wang, Shuqin Wei[‡], Zeyao Li[‡], Kaiyu Xue, Rui Bai, Tianlei Zhang[*]**

4 *Shaanxi Key Laboratory of Catalysis, School of Chemical & Environment Science, Shaanxi*

5 *University of Technology, Hanzhong, Shaanxi 723001, P. R. China*

6 # Abstract

7 Organosulfates (OSs) are key components of atmospheric aerosols and serve as tracers for

8 secondary organic aerosol (SOA) formation. Among these, lactic acid sulfate (LAS) has been

9 increasingly detected in the atmosphere. However, its molecular formation pathways and its role in

10 new particle formation (NPF) remain poorly understood. In this work, we investigate the gas-phase

11 formation mechanism of LAS via the reaction between lactic acid (LA) and SO$_3$, and assess its

12 impact on sulfuric acid-ammonia (SA-A) driven NPF using quantum chemical calculations and

13 Atmospheric Cluster Dynamics Code (ACDC) kinetic modeling. Our results show that SA and H$_2$O

14 significantly catalyze the LA-SO$_3$ reaction, enhancing the effective rate coefficient by 7-10 orders

15 of magnitude within the temperature range of 280-320 K. Further molecular-level analysis using the

16 ACDC reveals that LAS not only significantly enhances the clustering stability of SA and A up to

17 10^8-fold, but also plays a significant and direct role in SA-A nucleation under conditions typical of

18 forested and agricultural regions. Notably, LAS-SA-A clusters contribute to 97% of the overall

19 cluster formation pathways in regions with high LAS concentrations like Centreville, Alabama.

20 Additionally, our findings show that the nucleation potential of LAS-SA-A clusters is stronger than

21 that of LA-SA-A clusters, aligning with field observations, even though LAS concentrations are

22 typically three orders of magnitude lower than LA. These findings imply that OSs formed through

23 SO$_3$ consumption may significantly contribute to the enhanced NPF rates observed in continental

24 regions.

[*] Corresponding authors Tel: +86-0916-2641083, Fax: +86-0916-2641083.
 E-mail addresses: ztianlei88@l63.com (T. L Zhang)
[‡] Shuqin Wei and Zeyao Li contributed equally to this work.

1 Introduction

Atmospheric aerosol particles pose significant risks to public health, adversely affecting both the respiratory and cardiovascular systems (Anderson et al., 2012; Xing et al., 2016; Zhang et al., 2023b). Beyond health implications, these particles contribute to global warming by reducing visibility and disrupting the Earth's radiative balance (Lund et al., 2019; Zheng et al., 2018). As a major source of atmospheric aerosols, new particle formation (NPF), accounts for over 50% of the total particle number concentration and is strongly associated with severe haze events in megacities across China (Kulmala et al., 2004; Brean et al., 2020). Despite its significance, accurately characterizing the NPF process remains a considerable challenge, primarily due to limitations in current measurement techniques and an incomplete comprehension of the underlying mechanisms. While field observations and CLOUD chamber experiments (Kulmala et al., 2004; Dai et al., 2023; Lee et al., 2019; Hirsikko et al., 2011; Zhang et al., 2015) have provided valuable insights, they are insufficient to fully elucidate these processes. To address these gaps, a molecular-level approach is essential, as it allows for a more precise understanding of nucleation mechanisms (Yang et al., 2021; Li et al., 2017). This approach enables the detailed determination of molecular cluster geometries, the strengths of intermolecular interactions, and the pathways of cluster formation (Long et al., 2013; Zu et al., 2024b; Rong et al., 2020b). Such molecular insights are critical to evaluating the impacts of aerosols on the atmosphere and for devising effective strategies to mitigate haze formation.

Gaseous sulfuric acid (SA), derived from the oxidation of SO_2, has long been recognized as a key NPF precursor (Kirkby et al., 2011; Zhao et al., 2024). Molecular-level studies have shown that various nucleation precursors, including water (H_2O) (Zhang et al., 2012b), ammonia (A) (Kirkby et al., 2011; Zhang et al., 2015), methylamine (MA) (Shen et al., 2020), dimethylamine (DMA) (Cai et al., 2021; Kurtén et al., 2008), monoethanolamine (MEA) (Shen et al., 2019), piperazine (PZ) (Ma et al., 2019) and iodic acid (Sipilä et al., 2016), are involved in SA-driven binary nucleation, which serves as a primary initiator of NPF. However, binary nucleation mechanisms alone cannot fully account for the discrepancies observed between measured and modeled global NPF rates (Hodshire et al., 2019; Kirkby et al., 2016), suggesting the involvement of additional gaseous species. Then plenty of low weight molecular organic acids such as glycolic acid (Zhang et al., 2017), malonic acid (Zhang et al., 2018) and pyruvic acid (Tsona Tchinda et al., 2022) also exhibit

54 enhancement effects on ternary nucleation driven by SA-A nucleation system through catalytic

55 mechanisms. Despite recognizing the enhancement provided by SA-A-driven ternary nucleation,

56 the nucleation rates predicted by these mechanisms still fall short when compared to field

57 observations (Kirkby et al., 2016; Hodshire et al., 2019; Yin et al., 2021). The persistent

58 underestimation underscores the need for further investigation into the role of additional gaseous

59 species to better understand the complex mechanisms driving NPF.

60 Organosulfates (OSs), formed through the chemical transformation of organic acids, constitute

61 a major portion of organosulfur species in atmospheric aerosols, contributing 5-30% to the organic

62 mass in PM_{10} (Sun et al., 2025; Brüggemann et al., 2017). These compounds are prevalent in

63 atmospheric particles and are commonly employed as markers to track the formation of secondary

64 organic aerosols (SOAs) in environmental research (Tan et al., 2022; Zhang et al., 2012a; Froyd et

65 al., 2010a; Brüggemann et al., 2017; Mutzel et al., 2015; Glasius et al., 2017). Recent research has

66 led to the identification and characterization of various OSs in fine particulate matter samples from

67 regions including the United States, China, Mexico City and Pakistan (Hettiyadura et al., 2017;

68 Wang et al., 2018; Olson et al., 2011). Meanwhile, studies suggest that the cycloaddition of SO_3 to

69 organic acids could be a key mechanism for OSs formation resulting in compounds with lower vapor

70 pressures than their parent carboxylic acids and increased inter-molecular interaction sites (Smith

71 et al., 2020; Tan et al., 2020; Yao et al., 2020; Zhang et al., 2023a). Notably, lactic acid sulfate (LAS)

72 has been identified as the dominant OSs species across all these field observations (Darer et al.,

73 2011; Riva et al., 2015; Kundu et al., 2013). However, the specific formation mechanism of LAS

74 from the reaction of lactic acid (LA) with SO_3 remains largely unexplored. Additionally, SA and

75 water (H_2O) (Tan et al., 2022; Zhang et al., 2025; Li et al., 2018b), both prevalent in the atmosphere,

76 act as strong hydrogen atom donors/acceptors, facilitating proton transfer reactions and potentially

77 catalyzing the LA-SO_3 reaction.

78 The reaction products of SO_3 with major atmospheric trace species have been shown proven

79 to significantly influence the formation of NPF. For instance, compounds such as sulfamic acid (Li

80 et al., 2018a), oxalic sulfuric anhydride (Yang et al., 2021), methyl hydrogen sulfate (Liu et al.,

81 2019), glyoxylic sulfuric anhydride (Rong et al., 2020a) and formic acid sulfate (Wang et al., 2025),

82 generated through reactions of SO_3 with A, oxalic acid, methanol, glyoxylic acid and formic acid,

83 all exhibit catalytic effects on NPF in aerosols. Structurally, LAS, the product of the SO_3 + LA

84   reaction, contains both -COOH and -SO$_3$H functional groups, which facilitate additional hydrogen

85   bonding with atmospheric particle precursors (Yao et al., 2020). However, the role of LAS in

86   enhancing SA-A nucleation remains underexplored, limiting our ability to comprehensively

87   evaluate its impact on NPF processes. Furthermore, LA, a highly oxidized α-hydroxy acid with both

88   -OH and -COOH groups (Mochizuki et al., 2019), can enhance the stability of SA-A clusters and

89   facilitate NPF (Li et al., 2017). Given its relatively larger atmospheric concentrations, particularly

90   in regions with elevated organic acid pollution, LA may also significantly influence NPF. So,

91   understanding the distinct contributions of LAS and LA to SA-A nucleation is crucial, as this will

92   advance our understanding of NPF events, particularly in agricultural and forested regions.

93   In this work, we utilized quantum chemical calculations together with master equation analysis

94   to investigate the gas-phase reaction of SO$_3$ with LA that forms LAS, with H$_2$O and SA serving as

95   catalysts. The role of LAS in enhancing SA-A nucleation was then explored by examining the

96   formation mechanisms of the (LAS)$_x$(SA)$_y$(A)$_z$ ($0 \leq z \leq x + y \leq 3$) system using the Atmospheric

97   Clusters Dynamic Code (ACDC) kinetic model. Additionally, the potential influence of LAS on

98   atmospheric new particle formation (NPF) was assessed across diverse global regions. Finally, a

99   comparative study of LA and LAS was also conducted to elucidate the respective roles of organic

100   acids and OSs in enhancing SA-A nucleation, focusing on the formation mechanisms of both LA-

101   SA-A and LAS-SA-A systems.

2 Methodology

2.1 Quantum chemical calculations

104   The gas-phase reaction of SO$_3$ with LA to form LAS, both in the absence and presence of

105   H$_2$O and SA as catalysts, was systematically optimized and calculated using the Gaussian 09

106   program (Faloona et al., 2009) at the M06-2X/6-311++G(2df,2pd) level (Stewart, 2007; Walker

107   et al., 2013). Intrinsic reaction coordinate analyses (Hratchian and Schlegel, 2005) were carried

108   out at the same computational level to verify the connection between transition states and their

109   respective pre-reactive complexes and products. Furthermore, single-point energy calculations

110   were refined at the CCSD(T)-F12/cc-pVDZ-F12 level with the ORCA program (Neese, 2012),

111   employing the optimized geometries as input.

112   To identify the global minimum energy configurations of (SA)$_x$(A)$_y$(LAS)$_z$ clusters (where 0

113 ≤ y ≤ x + z ≤ 3), we utilized the ABCluster program (Zhang and Dolg, 2016) to systematically

114 generate initial structures for various clusters combinations. Specifically, using the ABCluster

115 procedure and the CHARMM force field, a diverse set of initial structures $n \times 1000$ ($1 \leq n \leq 3$) were

116 randomly produced. Initially, the primary structures were optimized and their energies were ranked

117 using the PM6 method in MOPAC 2016 (Partanen et al., 2016; Stewart, 2007). After the initial

118 sampling, considering the excellent performance of the M06-2X method in accurately

119 characterizing the geometries of atmospheric clusters (Walker et al., 2013; Lu et al., 2020), up to

120 1000 favorable configurations were selected for rigorous re-optimization at the M06-2X/3-21G*

121 level of theory. Subsequently, the 100 lowest-energy configurations were further optimized using

122 the M06-2X/6-31G(d, p) level of theory, from which the 10 configurations with the lowest energies

123 were identified. Finally, to accurately determine the global minimum, the M06-2X/6-311++G($2df$,

124 $2pd$) method was applied to refine these 10 lowest-energy configurations.

125 **2.2 Rate coefficients calculations**

126 Rate constants for the SO_3 + LA reaction, both without and with H_2O and H_2SO_4 as catalysts,

127 were determined via Rice-Ramsperger-Kassel-Marcus (RRKM) theory (Glowacki et al., 2012;

128 Wardlaw and Marcus, 1984) within the Master Equation (ME/RRKM) framework in MESMER

129 (Master Equation Solver for Multi-Energy Well Reactions) code (Glowacki et al., 2012;

130 Klippenstein and Marcus, 1988). Specifically, in the MESMER calculations, the rate constants for

131 the barrierless formation of pre-reactive complexes from reactants were determined using the

132 Inverse Laplace Transform (ILT) method (Horváth et al., 2020), whereas the subsequent conversion

133 of these complexes to products via transition states was evaluated using RRKM theory (Mai et al.,

134 2018). The ILT method and RRKM theory can be represented in Eqs. (1) and (2), respectively:

$$k^{\infty}(\beta) = \frac{1}{Q(\beta)} \int_0^{\infty} k(E)\rho(E)\exp(-\beta E)dE$$

135 (1)

$$k(E) = \frac{W(E - E_0)}{h\rho(E)}$$

136 (2)

137 Here, h represents Planck's constant, $\rho(E)$ indicates the density of accessible states for the reactant

138 at energy E, E_0 is the reaction threshold energy and $W(E-E_0)$ refers to the rovibrational states of the

139 transition state, excluding motion along the reaction coordinate. Geometries, vibrational frequencies,

140 and rotational constants were obtained at the M06-2X/6-311++G($2df$,$2pd$) level, with single-point

141 energies refined at the method of CCSD(T)-F12/cc-pVDZ-F12.

142 **2.3 ACDC kinetics simulation**

143   The ACDC was utilized to investigate the molecular-level collision coefficient (β, cm^3 s^{-1}),

144 evaporation coefficient (γ, s^{-1}) and cluster formation rates (J, cm^{-3} s^{-1}). Thermodynamic parameters

145 and structural information for cluster formation, obtained from quantum chemical calculations

146 performed by M06-2X/6-311++G(2df,2pd), served as input parameters for the ACDC model. The

147 MATLAB-R2014a platform, leveraging its odel5s solver (Shampine and Reichelt, 1997), performed

148 numerical integration of the birth-death equation for the ACDC model, thereby elucidating the

149 kinetics of cluster growth over time. The general form of the birth-death equation for the

150 concentration c_i of cluster i given by,

$$\frac{dc_i}{dt} = \frac{1}{2}\sum_{j<i}\beta_{j,(i-j)}c_j c_{(i-j)} + \sum_{j}\gamma_{(i+j)\to i}c_{i+j} - \sum_{j}\beta_{i,j}c_i c_j - \frac{1}{2}\sum_{j<i}\gamma_{i\to j}c_i + Q_i - S_i \quad (3)$$

152   In this formulation, $\beta_{i,j}$ corresponds to the collision frequency factor between clusters of sizes

153 i and j, $\gamma_{(i+j)\to i}$ quantifies the fragmentation rate of composite clusters into their constituent

154 monomers i and j. The system's open nature is accounted for through Q_i, representing the external

155 flux of cluster i, and S_i, characterizing its removal rate. Sensitivity tests were conducted by varying

156 the condensation sink (Cs) from $6 \times 10^{-4} \sim 6 \times 10^{-2}$ s^{-1}, indicating that the Cs exerted minimal

157 influence on the main conclusions (Fig. S11). Therefore, the Cs was set to a representative value of

158 2.6×10^{-3} for all subsequent calculations (Liu et al., 2021). Additionally, (LAS)$_4$(A)$_3$, (LAS)$_4$(A)$_4$,

159 (LAS)$_2$(SA)$_2$(A)$_3$, (LAS)$_2$(SA)$_2$(A)$_4$, (LAS)(SA)$_3$(A)$_3$, (LAS)(SA)$_3$(A)$_4$, (SA)$_4$(A)$_3$ and (SA)$_4$(A)$_4$

160 clusters are acting as boundary clusters for LAS-SA-A system. Also, the details of the contribution

161 of LAS to SA-A nucleation was estimated in the first part of the Supplement.

3   Results and discussions

162

3.1 Formation of LAS via the reaction of SO₃ with LA

163

164   In the direct cycloaddition pathway (Channel LAS) illustrated in Fig. 1, the hydroxyl (-OH)

165 group of LA reacts with the sulfur atom of SO$_3$, leading to the formation of LAS via proton transfer

166 from LA to SO$_3$. However, the resulting SO$_3$···LA complex (denoted as IM) is thermodynamically

167 unstable, primarily due to the significant ring strain in the four-membered structure, exhibiting a

168 relative Gibbs free energy of 5.6 kcal·mol^{-1}. The Gibbs free energy barrier for this reaction is

169   calculated to be 22.3 kcal·mol^{-1}. As indicated in Table S5, the rate coefficients for Channel LAS are

170   extremely low, spanning from 1.35×10^{-26} to 6.21×10^{-25} cm^3·molecule^{-1}·s^{-1} across the temperature

171   range of 230-320 K. These values suggest that this pathway is both slow and thermodynamically

172   unfavorable for LAS formation under typical atmospheric conditions.

173   H_2O, highly abundant in the atmosphere with concentration around 10^{17} molecules·cm^{-3}

174   (Huang et al., 2015), serves as both a donor and acceptor of hydrogen bonds, and is widely

175   recognized for its ability to catalyze a wide range of proton transfer reactions. To assess its catalytic

176   effect on the formation of LAS, we examined the SO_3 + LA reaction in the presence of H_2O

177   (Channel WM), as illustrated in Fig. 1. This reaction can proceed via three possible sequential

178   bimolecular pathways: (*i*) SO_3···LA + H_2O, (*ii*) SO_3···H_2O + LA and (*iii*) LA···H_2O + SO_3.

179   Considering typical atmospheric concentrations of SO_3 (10^5 molecules·cm^{-3}) (Zhang et al., 2024),

180   LA (10^{12} molecules·cm^{-3}) (Li et al., 2017) and H_2O (10^{17} molecules·cm^{-3}) (Huang et al., 2015), the

181   calculated concentrations of SO_3···LA, SO_3···H_2O and LA···H_2O complexes at 298 K are 4.18 ×

182   10^{-2}, 5.80 × 10^3 and 2.32 × 10^8 molecules·cm^{-3}, respectively (see Table S2 in the Supplement).

183   These results suggest that Channel WM predominantly proceeds via the collision of LA···H_2O with

184   SO_3.

185   The free energy barrier for Channel WM is 7.8 kcal·mol^{-1}, which is 14.5 kcal·mol^{-1} lower than

186   the barrier for the uncatalyzed cycloaddition pathway. At the experimental concentration of H_2O

187   ([H_2O] = 10^{17} molecules·cm^{-3}) (Huang et al., 2015), the effective rate coefficient for the H_2O-

188   catalyzed reaction is 2.00×10^{-16} cm^3 molecule^{-1} s^{-1}, which is nine orders of magnitude greater than

189   the rate for the direct cycloaddition pathway (2.22×10^{-25} cm^3 molecule^{-1} s^{-1}). These results clearly

190   demonstrate that the H_2O-catalyzed LA + SO_3 reaction represents a significantly more favorable

191   route for LAS formation. Detailed effective rate coefficients for the H_2O-catalyzed reaction are

192   provided in Fig. 2(a).

193   SA is another abundant atmospheric species that efficiently donates and accepts hydrogen bond,

194   facilitating proton transfer (Yao et al., 2018; Tan et al., 2018) and potentially catalyzing the LA +

195   SO_3 reaction. As shown in Fig. 1, SA is significantly more effective than H_2O in promoting LAS

196   formation via cycloaddition. Specifically, SA increases the stabilization energy of the SO_3···LA

197   complex by 7.1 kcal·mol^{-1}, 5.0 kcal·mol^{-1} greater than the stabilization provided by H_2O and reduces

198   the distance between the oxygen atom of the -OH group in LA and the sulfur atom in SO_3 by 0.09

199 Å in the SO$_3$···LA···SA complex. As compared with six-membered ring transition state TS$_{WM}$, the

200 transition state TS$_{SA}$ shows eight-membered ring structure, which reduces the ring tension greatly.

201 So, from an energetic point of view, SA lowers the Gibbs free energy barrier to 3.5 kcal·mol^{-1}, 4.3

202 kcal·mol^{-1} lower than the barrier observed for the H$_2$O-catalyzed pathway. The effective rate

203 coefficients for the SA ([SA] = 10^7 molecules·cm^{-3})-catalyzed reaction (k'_{SA}) is 4-5 orders of

204 magnitude higher than that for the H$_2$O-catalyzed pathway (k'_{WM}) at 100 % relative humidity,

205 indicating that SA is kinetically more favorable, particularly at altitudes of 5-10 km. Thus, SA

206 predominantly catalyzes the SO$_3$ + LA reaction, significantly contributing to the gas-phase loss of

207 SO$_3$ in LA-rich atmospheric regions.

208 Previous theoretical studies have indicated that atmospheric acids can catalyze the hydrolysis

209 of SO$_3$ to form SA (Hazra and Sinha, 2011; Cheng et al., 2022; Long et al., 2013; Lv et al., 2019).

210 In this context, the potential catalytic role of LA in SO$_3$ hydrolysis was also explored. The potential

211 energy surface (PES) for this reaction is presented in Fig. S2, with the effective rate coefficients

212 compared to those for SO$_3$ hydrolysis catalyzed by SA, HNO$_3$, HCOOH, and OA. As shown in Fig.

213 2(b), LA predominantly catalyzes SO$_3$ hydrolysis within the temperature range of 280-320 K at a

214 concentration of 1.0×10^{12} molecules·cm^{-3}. Besides, given the current lack of atmospheric field data

215 on gas-phase LAS and lactic acid sulfuric anhydride (LASA, the product from the reaction between

216 SO$_3$ and the carboxyl group of LA, Fig. S1), thermodynamic equilibrium calculations were used to

217 estimate their concentrations and assess their potential impacts on atmospheric NPF. Modeling

218 results suggest LAS concentrations of 10^3-10^5 molecules·cm^{-3}, which is nine orders of magnitude

219 higher than that of LASA (ranging from 10^{-6}-10^{-4} molecules·cm^{-3}). This suggests that LAS has

220 significantly more atmospheric relevance than LASA, with a correspondingly higher potential to

221 influence NPF. Detailed calculations and further insights are provided in Table S4.

3.2 Enhancing effect of LAS on SA-A-driven NPF

223 The role of LAS in promoting SA-A-driven NPF process was thoroughly examined. Initially,

224 potential interaction sites between LAS and SA-A clusters were identified through molecular

225 analyses. Next, the stable structures and thermodynamic stabilities of various (LAS)$_x$(SA)$_y$(A)$_z$ ($y \leq$

226 $x + z \leq 3$) clusters were characterized, providing insight into their structural integrity. Building on

227 these findings, the nucleation mechanism of the SA-A-LAS system was investigated, with a

228 particular focus on the impact of temperature and precursor concentrations on LAS-mediated NPF

229 processes. Finally, the atmospheric implications of LAS-enhanced SA-A nucleation were evaluated,

230 especially in forested and agricultural-developed regions.

3.2.1 Cluster stability analysis

232 Stable cluster formation is primarily driven by strong interactions between nucleation

233 precursors (Lu and Chen, 2012). To assess the binding potential of LAS with the SA-A cluster, the

234 electrostatic potential (ESP)-mapped molecular van der Waals surface was calculated to identify

235 key interaction sites. As shown in Fig. 3, the hydrogen atom of the -SO$_3$H moiety in LAS exhibits

236 a positive ESP of +78.73 kcal·mol^{-1}, suggesting its role as a hydrogen bond donor that can interact

237 with the double-bonded oxygen atom of SA or the nitrogen atom of A, both of which act as hydrogen

238 bond acceptors. Additionally, the double-bonded oxygen in LAS, with a negative ESP of -32.51

239 kcal·mol^{-1}, can act as a hydrogen-bond acceptor, interacting with the hydroxyl hydrogen of SA (-

240 OH) or the hydrogen of A. These intermolecular interactions imply that LAS enhances nucleation

241 efficiency between SA and A during aerosol nucleation, thereby stabilizing the resulting molecular

242 clusters. Based on the ESP analysis, the most stable configurations of (LAS)$_x$(SA)$_y$(A)$_z$ ($z \leq x + y \leq$

243 3) clusters were identified (Fig. S3), with the observed interaction sites in the ternary clusters

244 corresponding well to the ESP predictions.

245 To quantitatively evaluate the binding strength of LAS within binary SA-A-based clusters, the

246 Gibbs free energies (ΔG, kcal·mol^{-1}, Table S7) for the (LAS)$_x$(SA)$_y$(A)$_z$ ($z \leq x + y \leq 3$) clusters were

247 calculated at temperatures of 238.15 K, 258.15 K, 278.15 K and 298.15 K. All clusters exhibited

248 negative ΔG values, confirming thermodynamic favorability. Importantly, ternary SA-A-LAS

249 clusters consistently demonstrated lower ΔG values compared to their binary counterparts,

250 suggesting that the presence of LAS reinforces the stability of SA-A clusters. Further analysis of

251 stability at 278.15 K was carried out by examining total evaporation rates ($\sum \gamma$), derived from cluster

252 ΔG values (Table S7) and collision rates (β, Table S8), as summarized in Fig. 4. Previous research

253 indicates that lower $\sum \gamma$ are indicative of greater cluster stability (Li et al., 2024; Zu et al., 2024a).

254 At 278.15 K, clusters incorporating LAS exhibit a lower $\sum \gamma$ compared to those composed solely of

255 SA and A molecules. For example, the $\sum \gamma$ values for the (A)$_1$·(LAS)$_1$ (1.19 × 10^4 s^{-1}) and

256 (A)$_3$·(LAS)$_3$ (8.64 × 10^{-8} s^{-1}) clusters were 3.1-10^8 times lower than those for the (SA)$_1$·(A)$_1$ (3.73

257 × 10^4 s^{-1}) and (SA)$_3$·(A)$_3$ (3.28 × 10^1 s^{-1}) clusters. Similarly, the $\sum \gamma$ values of the (SA)$_1$·(A)$_3$·(LAS)$_2$

258 (1.99 × 10^0 s^{-1}) and (SA)$_2$·(A)$_3$·(LAS)$_1$ (2.29 × 10^{-4} s^{-1}) clusters at 278.15 K were found to be 10^1-

259   10^5 times lower than the most stable binary cluster, $(SA)_3 \cdot (A)_3$ (3.28×10^1 s^{-1}). Moreover, these

260   clusters exhibited $\beta C/\sum \gamma$ ratios greater than 1 (Table S11), suggesting a favorable balance between

261   cluster growth and evaporation. Similar trends in ΔG and $\sum \gamma$ were observed across the other

262   temperatures studied, including 238.15 K, 258.15 K and 298.15 K. Taken together, the ΔG and $\sum \gamma$

263   analyses provide strong evidence that LAS incorporation enhances SA-A cluster stability, thereby

264   increasing their likelihood of participating in nucleation events.

265   **3.2.2 Cluster formation pathways**

266   To investigate the detailed nucleation pathways of LAS in the formation of SA-A clusters,

267   ACDC simulation were conducted at 278.15 K, with the concentrations of [SA] (10^6 molecules·cm$^-$

268   ^{3}), [A] (10^9 molecules·cm^{-3}) and [LAS] (10^5 molecules·cm^{-3}). The results are presented in Fig. 5(a),

269   illustrating two distinct mechanisms for cluster growth. The first pathway (depicted by black arrows)

270   corresponds to pure SA-A clustering, starting from the $(SA)_1 \cdot (A)_1$ dimer. Subsequent stepwise

271   addition of SA or A monomers drives the assembly of progressively larger and more stable clusters

272   such as $(SA)_3 \cdot (A)_3$, which eventually exit the system. The second pathway (depicted by blue arrows)

273   includes clusters containing LAS, in which LAS performs two distinct roles: one as a "catalyst" and

274   the other as a "participant". When LAS acts as a "catalyst", the $(SA)_1 \cdot (A)_2 \cdot (LAS)_1$ trimer collides

275   with the SA monomer, forming the $(SA)_2 \cdot (A)_2 \cdot (LAS)_1$ cluster. Subsequently, LAS evaporates from

276   the cluster, leaving behind the $(SA)_2 \cdot (A)_2$ cluster. Meanwhile, when LAS acts as a "participant",

277   collisions between the $(SA)_1 \cdot (A)_1$ dimer and LAS monomers lead to the assembly of the

278     $(SA)_1 \cdot (A)_1 \cdot (LAS)_1$ cluster. This trimer then undergoes further collisions with either an SA or A

279   monomer, producing the $(SA)_2 \cdot (A)_3 \cdot (LAS)_1$ cluster, which ultimately grows out of the system.

280   These dual roles of LAS in SA-A clusters are observed across other temperatures of 298.15 K,

281   238.15 K and 258.15 K; however, at lower temperatures, such as 238.15 K, the LAS-involved

282   pathway simplifies (as shown in Figs. S8, S9 and S10).

283   As shown in Fig. 5(b), the contributions of LAS to the SA-A nucleation process were examined

284   across a range of temperatures, with a focus on the nucleation mechanism that involves LAS

285   participation. As temperature increases, the influence of LAS-involved pathways becomes

286   progressively more dominant, due to the elevated vapor pressure of LAS raises its gas-phase

287   concentration, thereby promoting further cluster formation. At lower temperatures (238.15 and

288   258.15 K), SA-A clustering remains the dominant process, accounting for 73% of nucleation events,

289   while LAS-involved pathways contribute a modest 21%, because of the reduced collision frequency

290   of LAS. However, as the temperature rises to 278.15 K, LAS participation increases to 33%,

291   signaling a more prominent role in cluster growth. At 298.15 K, this contribution further rises to

292   49%, nearly double that observed at the lower temperatures. These results highlight the crucial role

293   of elevated temperatures in enhancing LAS's contribution to SA-A nucleation, emphasizing the

294   temperature-dependent amplification of LAS-driven cluster formation.

3.2.3 Atmospheric implications of LAS

296   In addition to temperature, the concentrations of precursors play a pivotal role in SA-A aerosol

297   nucleation. Atmospheric LAS concentrations exhibit considerable variability across different global

298   environments (Tan et al., 2022; Mochizuki et al., 2017; Ristovski et al., 2010; Hettiyadura et al.,

299   2017; Kanellopoulos et al., 2022). For example, lower LAS concentrations, ranging from 1.00×10^4

300   to 8.34×10^5 molecules·cm^{-3}, are found in regions such as eucalypt forest (Ristovski et al., 2010),

301   Mt. Tai (China) (Mochizuki et al., 2017) and Athens (Kanellopoulos et al., 2022). In contrast, higher

302   LAS concentrations have been recorded in Centreville, Alabama (1.77×10^6 molecules·cm^{-3})

303   (Hettiyadura et al., 2017), with peak levels in Patra (Kanellopoulos et al., 2022) , reaching up to

304   1.70×10^7 molecules·cm^{-3}. Similarly, the concentrations of SA and A vary, with SA ranging from

305   10^4-10^7 molecules·cm^{-3} (Zhang et al., 2024; Ding et al., 2019), and A ranging from 10^7-10^{11}

306   molecules·cm^{-3} (Wu et al., 2017; Luo et al., 2014). Elevated concentrations of these species are

307   particularly prominent in regions such as northern China, the Midwestern United States, and

308   agricultural areas in Europe. Based on field observations of LAS, SA and A concentrations, the

309   contribution of LAS to SA-A nucleation was systematically assessed. As illustrated in Fig. S18, the

310   impact of LAS on the SA-A system is primarily governed by the concentrations of LAS and SA,

311   with minimal dependence on [A]. Consequently, Fig. 6 illustrates how the contribution ratio of LAS

312   varies with different concentrations of SA and LAS, under the previously identified favorable high-

313   temperature condition of 278.15 K.

314   The three pie charts in the upper map illustrate the changing contribution of LAS to SA-A

315   aerosol nucleation as SA concentration increases from 3.00×10^4 to 6.00×10^4 molecules·cm^{-3}, with

316   a corresponding decrease in LAS contribution as [SA] rises. In regions characterized by low SA

317   concentrations (3.00×10^4 molecules·cm^{-3}), such as Hyytiälä, nucleation is predominantly driven

318   by the LAS-SA-A pathway, contributing approximately 93%. However, at higher SA concentrations

319 (up to 2.00×10^6 molecules·cm^{-3}), such as on the west coast of Ireland (O'dowd et al., 2002), the

320 LAS contribution drops from 93% to 33%. At even higher SA levels (up to 1.00×10^7 molecules·cm^{-3}

321 ^{3}), LAS-involved pathways account for only 18% of the total nucleation flux, as observed in Beijing,

322 China (Wang et al., 2011). In contrast, environments with typically high SA concentrations, such as

323 urban and industrial areas, promote SA-A self-aggregation nucleation, thereby diminishing the

324 relative contribution of LAS (Fig. S10). These findings highlight that lower [SA] levels substantially

325 amplify the contribution of LAS contribution to SA-A aerosol nucleation.

326   The contribution of LAS to SA-A aerosol nucleation increases with LAS concentration,

327 ranging from 1.00×10^4 to 1.77×10^6 molecules·cm^{-3}, as shown in the pie chart below the map.

328 This pattern indicates a positive correlation between LAS concentration and its contribution to

329 nucleation. In regions with low LAS concentrations (1.00×10^4 molecules·cm^{-3}), such as eucalypt

330 forests (Ristovski et al., 2010), LAS-mediated pathways account for only 15% of the total nucleation

331 flux. While LAS contributes to the initial stages of cluster formation, it subsequently evaporates

332 from the pre-nucleation cluster, ultimately functioning in a catalyst-like capacity (Fig. S16). In areas

333 with moderate LAS concentrations, such as Athens (8.34×10^5 molecules·cm^{-3}) (Kanellopoulos et

334 al., 2022) and Mt. Tai (1.00×10^5 molecules·cm^{-3}) (Mochizuki et al., 2017), LAS contribution

335 increases substantially, rising from 15% to 73%. At high [LAS], as observed in the Centreville,

336 Alabama (1.77×10^6 molecules·cm^{-3}) (Hettiyadura et al., 2017), LAS-driven nucleation becomes

337 dominant, resulting in a 'participant' synergistic nucleation mechanism that works like 'hand in

338 hand' (Fig. S17), contributing up to 97 % of the total nucleation rate. These findings underscore that

339 elevated LAS concentrations significantly enhance SA-A nucleation. Thus, in regions characterized

340 by high T, low [SA], high [A] and high [LAS], especially in agricultural-developed areas and

341 forested areas, the LAS contribution to SA-A aerosol nucleation can be substantial.

342 **3.3 The comparison of enhancement effect between LAS and LA**

343   To evaluate the relative enhancing effects of LA versus LAS in the typical SA-A-driven

344 nucleation. The ΔG (pink histograms) and $\sum\gamma$ (red points) of the $(LAS)_x(SA)_y(A)_3$ and

345 $(LA)_x(SA)_y(A)_3$ ($x = 0 - 3$, $x + y = 3$) clusters at 278.15 K are presented in Fig. 7(a) as a comparison.

346 The $(SA)_3(A)_3$ cluster, the thermodynamic minimum of the SA-A system (Chen et al., 2025; Li et

347 al., 2020), was chosen as a reference for comparison. Relative to this baseline, $(LA)_{1-3}(SA)_{0-2}(A)_3$

348 clusters consistently exhibited higher ΔG values, elevated by roughly 18.36-41.94 kcal·mol^{-1}. In

349   contrast, $(LAS)_{1-3}(SA)_{0-2}(A)_3$ clusters were slightly more stable, differing from the reference by only

350   0.09-5.80 kcal·mol^{-1}. This suggests that LAS incorporation leads to a slight stabilization of the

351   cluster relative to LA.

352   Moreover, the evaporation rate ($\sum\gamma$) of the $(Org)_x(SA)_y(A)_3$ (Org = LA and LAS; x =1-3，x +

353   y =3) clusters do not exhibit a simple relationship with the proportion of organic components within

354   the clusters. The highest $\sum\gamma$ was observed for the $(Org)_2·(SA)_1·(A)_3$ (Org = LA and LAS) clusters,

355   regardless of whether LA or LAS was used. For the $(LAS)_1·(SA)_2·(A)_3$ and $(LAS)_3·(A)_3$ clusters,

356   the $\sum\gamma$ ranged from 10^{-4} to 10^{-1} s^{-1}, lower than that of the $(SA)_3·(A)_3$ cluster, indicating that replacing

357   one or three SA molecules with LAS enhances the thermodynamic stability of the clusters. In

358   contrast, the $\sum\gamma$ of the LA-SA-A clusters were found to be higher than those of the corresponding

359   LAS-SA-A and $(SA)_3·(A)_3$ clusters, as displayed in Fig. 7(a). The LAS-SA-A clusters exhibit more

360   negative ΔG values and lower $\sum\gamma$, suggesting that their formation is thermodynamically more

361   favorable than that of the LA-SA-A system. This enhanced stability can be attributed to stronger

362   interactions between LAS and SA-A systems relative to those between LA and SA-A. Based on

363   these results, we can conclude that LAS, produced through the LA + SO$_3$ reaction, more effectively

364   stabilizes the SA-A system than LA itself.

365   Fig. 7(b) illustrates the variation in the cluster formation rate (J) and enhancement strength (R)

366   as a function of [LAS] and [LA] at 278.15 K, under the condition of [SA] = 10^6 molecules·cm^{-3} and

367   [A]=10^9 molecules·cm^{-3}. In the LAS-SA-A system, J increases sharply with rising [LAS],

368   particularly when [LAS] exceeds 10^5 molecules·cm^{-3}. As [LAS] grows from 10^5 to 10^6

369   molecules·cm^{-3}, J for the LAS-SA-A system rises by three orders of magnitude, whereas in the LA-

370   SA-A system, J exhibits only a modest increase from 3.36×10^{-9} to 1.12×10^{-8} cm^{-3} s^{-1}, consistent

371   with the corresponding increase in [LA] (Fig. 7b). Although LAS concentrations are typically three

372   orders of magnitude lower than LA (Tan et al., 2022), LAS exerts a substantially stronger

373   enhancement effect in SA-A-driven nucleation. These contrasting trends are primarily due to the

374   combined influence of cluster thermodynamic properties ΔG and $\sum\gamma$, and the concentrations of

375   organic species within the respective systems. The sharp increase in J for the LAS-SA-A system

376   stems from the favorable ΔG and low $\sum\gamma$ of the $(LAS)_x(SA)_y(A)_z$ clusters, along with the relatively

377   high non-equilibrium concentration of LAS. In contrast, the less favorable ΔG and higher $\sum\gamma$ of the

378     $(LA)_x(SA)_y(A)_z$ clusters limit the kinetic efficiency of the LA-SA-A system, even at elevated [LA].

379　　　This study reveals that the reaction of LA and SO_3 generates LAS which acts as an effective

380　atmospheric nucleation precursor and significantly accelerates SA-A nucleation. Consequently,

381　atmospheric LA can react with part of SO_3, potentially accounting for the relatively low observed

382　low SA concentration, while the generated LAS markedly promotes SA-A-driven NPF under such

383　conditions. To date, the effects of hydroxy acids and their derivatives on atmospheric NPF have not

384　been comprehensively investigated. The mechanism proposed here offers a general approach to

385　evaluate the roles of these acids, like 2-Methylglyceric acid, aromatic acids and their derivates,

386　influence atmospheric nucleation processes. Incorporating this novel OSs pathways into

387　contemporary atmospheric models will advance the quantitative understanding of OSs'

388　contributions to aerosol formation. Furthermore, OSs originating from secondary processes, such as

389　gas-phase chemical reactions, deserve further observation and evaluation.

390　4　Conclusions

391　　　In this study, quantum chemical calculations, master equation analysis, and the ACDC kinetic

392　model were employed to investigate the cycloaddition reaction between SO_3 and LA, the role of

393　LAS in SA-A nucleation, and its impact on NPF.

394　　　Quantum chemical results in the gas phase indicate that SA and H_2O effectively lower the

395　reaction barriers for LAS formation from the LA-SO_3 reaction, functioning as catalysts and even

396　enabling a barrierless reaction. The effective rate coefficient for the SO_3-LA reaction catalyzed by

397　SA (10^7 molecules·cm^{-3}) is 4-5 times higher than the pathway catalyzed by H_2O (10^{17} molecules·cm^{-}

398　^{3}), making it more effective, particularly at altitudes of 5-10 km. Additionally, the effective rate

399　coefficients for LA (10^{12} molecules·cm^{-3}) catalyzing the $SO_3 + H_2O \rightarrow$ SA reaction is about 10^1-10^4

400　times larger than the corresponding values for SO_3 hydrolysis catalyzed by H_2SO_4 (10^7

401　molecules·cm^{-3}), HNO_3 (10^9 molecules·cm^{-3}), HCOOH (10^{11} molecules·cm^{-3}), and OA (10^9

402　molecules·cm^{-3}), indicating that LA primarily catalyzes SO_3 hydrolysis within the temperature

403　range of 280-320 K.

404　　　LAS, functioning as both a hydrogen-bond donor and acceptor, participates in SA-A-driven

405　ternary nucleation, directly interacting with SA and A. Gibbs free energy analysis demonstrates that

406　ternary SA-A-LAS clusters consistently exhibit lower ΔG values than their binary counterparts,

407　suggesting that LAS incorporation stabilizes the SA-A clusters. ACDC kinetic simulations further

408 demonstrate that LAS significantly enhances NPF, especially at low temperatures, low SA

409 concentration, and high A and LAS concentrations. In regions with elevated LAS concentrations,

410 such as Centreville, Alabama, particle formation rates can increase by up to 10^8-fold, with SA-A-

411 LAS clusters contributing up to 97% of the overall cluster formation pathways. It is noteworthy that

412 LAS not only acts as a catalyst in enhancing SA-A cluster stability but also directly participates in

413 nucleation. Moreover, LAS exerts a stronger enhancement effect than LA, making it a more

414 effective stabilizing agent for atmospheric NPF. These findings suggest that LAS plays a critical

415 role in enhancing SA-A-driven NPF in forested and agriculturally developed regions, providing

416 insights into previously unaccounted NPF sources and refining nucleation models.

417 This study deepens the understanding of OSs formation in organic acid-polluted regions and

418 underscores the potential contribution of other OSs to NPF. Neglecting the contribution of OSs in

419 the SA-A aerosol nucleation, particularly in forested and agricultural regions, may lead to an

420 underestimation of organic aerosol nucleation risks.

421 **Data availability**

422 Data will be made available on request.

423 **Author contribution**

424 RW: writing (original draft) and funding acquisition; SW: methodology, investigation, data

425 curation, visualization, data computation and writing (original draft); ZL: data curation,

426 methodology and investigation; KX: data curation, visualization and investigation; RB: data

427 curation and project administration; TZ: writing (review and editing) and funding acquisition. All

428 the authors contributed to revise the manuscript and approve the final version.

433 **Competing interests**

434 The authors declare that they have no known competing financial interests or personal

435 relationships that could have appeared to influence the work reported in this paper.

436 # Reference

437 Anderson, J. O., Thundiyil, J. G., and Stolbach, A.: Clearing the air: a review of the effects of particulate
438 matter air pollution on human health, J. Med. Toxicol., 8, 166-175, 2012.
439 Brean, J., Beddows, D. C. S., Shi, Z., Temime-Roussel, B., Marchand, N., Querol, X., Alastuey, A.,
440 Minguillón, M. C., and Harrison, R. M.: Molecular insights into new particle formation in Barcelona,
441 Spain, Atmos. Chem. Phys., 20, 10029-10045, 2020.
442 Brüggemann, M., Poulain, L., Held, A., Stelzer, T., Zuth, C., Richters, S., Mutzel, A., van Pinxteren, D.,
443 Iinuma, Y., Katkevica, S., Rabe, R., Herrmann, H., and Hoffmann, T.: Real-time detection of highly
444 oxidized organosulfates and BSOA marker compounds during the F-BEACh 2014 field study, Atmos.
445 Chem. Phys., 17, 1453-1469, 2017.
446 Cai, R., Yan, C., Yang, D., Yin, R., Lu, Y., Deng, C., Fu, Y., Ruan, J., Li, X., Kontkanen, J., Zhang, Q.,
447 Kangasluoma, J., Ma, Y., Hao, J., Worsnop, D. R., Bianchi, F., Paasonen, P., Kerminen, V. M., Liu, Y.,
448 Wang, L., Zheng, J., Kulmala, M., and Jiang, J.: Sulfuric acid-amine nucleation in urban Beijing, Atmos.
449 Chem. Phys. , 21, 2457-2468, 2021.
450 Chen, S. S., Li, R. R., Zhang, C. Y., Wei, S. Q., Wang, R., Chu, B. W., Zhang, X. M., Li, H., and Zhang,
451 T. L.: The enhanced role of formic acid on sulfuric acid-ammonia-driven nucleation in forest regions and
452 polluted city areas, J. Environ. Sci., 621-628, 2025.
453 Cheng, Y., Wang, R., Chen, Y., Tian, S., Gao, N., Zhang, Z., and Zhang, T.: Hydrolysis of SO_3 in small
454 clusters of sulfuric acid: mechanistic and kinetic study, ACS Earth and Space Chemistry, 6, 3078-3089,
455 2022.
456 Dai, L., Zhao, Y., Zhang, L., Chen, D., and Wu, R.: Particle number size distributions and formation and
457 growth rates of different new particle formation types of a megacity in China, J. Environ. Sci., 131, 11-
458 25, 2023.
459 Darer, A. I., Cole-Filipiak, N. C., O'Connor, A. E., and Elrod, M. J.: Formation and stability of
460 atmospherically relevant isoprene-derived organosulfates and organonitrates, Environ. Sci. Technol., 45,
461 1895-1902, 2011.
462 Ding, J., Zhao, P., Su, J., Dong, Q., Du, X., and Zhang, Y.: Aerosol pH and its driving factors in Beijing,
463 Atmos. Chem. Phys., 19, 7939-7954, 2019.
464 Faloona, I., Conley, S. A., Blomquist, B., Clarke, A. D., Kapustin, V., Howell, S., Lenschow, D. H., and
465 Bandy, A. R.: Sulfur dioxide in the tropical marine boundary layer: dry deposition and heterogeneous
466 oxidation observed during the pacific atmospheric sulfur experiment, J. Atmos. Chem., 63, 13-32, 2009.
467 Froyd, K. D., Murphy, S. M., Murphy, D. M., de Gouw, J. A., Eddingsaas, N. C., and Wennberg, P. O.:
468 Contribution of isoprene-derived organosulfates to free tropospheric aerosol mass, Proc. Natl. Acad. Sci.
469 U.S.A., 107, 21360-21365, 2010a.
470 Glasius, M., Hansen, A. M. K., Claeys, M., Henzing, B., Jedyńska, A., Kasper-Giebl, A., Kistler, M.,
471 Kristensen, K., Martinsson, J., Maenhaut, W., Nøjgaard, J., Spindler, G., Stenström, K., Swietlicki, E.,
472 Szidat, S., Simpson, D., and Yttri, K. E.: Composition and sources of carbonaceous aerosols in Northern
473 Europe during winter, Atmos. Environ., 173, 127-141, 2017.
474 Glowacki, D. R., Liang, C. H., Morley, C., Pilling, M. J., and Robertson, S. H.: MESMER: an open-
475 source master equation solver for multi-energy well reactions, J. Phys. Chem. A, 116, 9545-9560, 2012.
476 Hazra, M. K. and Sinha, A.: Formic acid catalyzed hydrolysis of SO3 in the gas phase: a barrierless
477 mechanism for sulfuric acid production of potential atmospheric importance, J. Am. Chem. Soc., 133,
478 17444-17453, 2011.
479 Hettiyadura, A. P. S., Jayarathne, T., Baumann, K., Goldstein, A. H., Gouw, J. A., Koss, A., Keutsch, F.
480 N., Skog, K., and Stone, E. A.: Qualitative and quantitative analysis of atmospheric organosulfates in

Centreville, Alabama, Atmos. Chem. Phys., 17, 1343-1359, 2017.

Hirsikko, A., Nieminen, T., Gagné, S., Lehtipalo, K., Manninen, H. E., Ehn, M., Hõrrak, U., Kerminen, V. M., Laakso, L., and McMurry, P.: Atmospheric ions and nucleation: a review of observations, Atmos. Chem. Phys., 11, 767-798, 2011.

Hodshire, A. L., Campuzano J. P., Kodros, J. K., Croft, B., Nault, B. A., Schroder, J. C., Jimenez, J. L., and Pierce, J. R.: The potential role of methanesulfonic acid (MSA) in aerosol formation and growth and the associated radiative forcings, Atmos. Chem. Phys., 19, 3137-3160, 2019.

Horváth, G., Horváth, I., Almousa, S. A. D., and Telek, M.: Numerical inverse laplace transformation using concentrated matrix exponential distributions, Performance Evaluation, 137, 102067, 2020.

Hratchian, H. P. and Schlegel, H. B.: Using hessian updating to increase the efficiency of a hessian based predictor-corrector reaction path following method, J. Chem. Theory Comput. 1, 61-69, 2005.

Huang, H. L., Chao, W., and Lin, J. J. M.: Kinetics of a Criegee intermediate that would survive high humidity and may oxidize atmospheric SO_2, Proc. Natl. Acad. Sci. U. S. A., 112, 10857-10862, 2015.

Kanellopoulos, P. G., Kotsaki, S. P., Chrysochou, E., Koukoulakis, K., Zacharopoulos, N., Philippopoulos, A., and Bakeas, E.: PM2.5-bound organosulfates in two Eastern Mediterranean cities: The dominance of isoprene organosulfates, Chemosphere, 297, 134103, 2022.

Kirkby, J., Curtius, J., Almeida, J., Dunne, E., Duplissy, J., Ehrhart, S., Franchin, A., Gagné, S., Ickes, L., Kürten, A., Kupc, A., Metzger, A., Riccobono, F., Rondo, L., Schobesberger, S., Tsagkogeorgas, G., Wimmer, D., Amorim, A., Bianchi, F., Breitenlechner, M., David, A., Dommen, J., Downard, A., Ehn, M., Flagan, R. C., Haider, S., Hansel, A., Hauser, D., Jud, W., Junninen, H., Kreissl, F., Kvashin, A., Laaksonen, A., Lehtipalo, K., Lima, J., Lovejoy, E. R., Makhmutov, V., Mathot, S., Mikkilä, J., Minginette, P., Mogo, S., Nieminen, T., Onnela, A., Pereira, P., Petäjä, T., Schnitzhofer, R., Seinfeld, J. H., Sipilä, M., Stozhkov, Y., Stratmann, F., Tomé, A., Vanhanen, J., Viisanen, Y., Vrtala, A., Wagner, P. E., Walther, H., Weingartner, E., Wex, H., Winkler, P. M., Carslaw, K. S., Worsnop, D. R., Baltensperger, U., and Kulmala, M.: Role of sulphuric acid, ammonia and galactic cosmic rays in atmospheric aerosol nucleation, Nature, 476, 429-433, 2011.

Kirkby, J., Duplissy, J., Sengupta, K., Frege, C., Gordon, H., Williamson, C., Heinritzi, M., Simon, M., Yan, C., Almeida, J., Tröstl, J., Nieminen, T., Ortega, I. K., Wagner, R., Adamov, A., Amorim, A., Bernhammer, A.-K., Bianchi, F., Breitenlechner, M., Brilke, S., Chen, X., Craven, J., Dias, A., Ehrhart, S., Flagan, R. C., Franchin, A., Fuchs, C., Guida, R., Hakala, J., Hoyle, C. R., Jokinen, T., Junninen, H., Kangasluoma, J., Kim, J., Krapf, M., Kürten, A., Laaksonen, A., Lehtipalo, K., Makhmutov, V., Mathot, S., Molteni, U., Onnela, A., Peräkylä, O., Piel, F., Petäjä, T., Praplan, A. P., Pringle, K., Rap, A., Richards, N. A. D., Riipinen, I., Rissanen, M. P., Rondo, L., Sarnela, N., Schobesberger, S., Scott, C. E., Seinfeld, J. H., Sipilä, M., Steiner, G., Stozhkov, Y., Stratmann, F., Tomé, A., Virtanen, A., Vogel, A. L., Wagner, A. C., Wagner, P. E., Weingartner, E., Wimmer, D., Winkler, P. M., Ye, P., Zhang, X., Hansel, A., Dommen, J., Donahue, N. M., Worsnop, D. R., Baltensperger, U., Kulmala, M., Carslaw, K. S., and Curtius, J.: Ion-induced nucleation of pure biogenic particles, Nature, 533, 521-526, 2016.

Klippenstein, S. J. and Marcus, R. A.: Unimolecular reaction rate theory for highly flexible transition states.2.Conventional coordinate formulas for the various possible fragment combinations: miscellaneous topics, J. Phys. Chem. C., 92, 5412-5417, 1988.

Kulmala, M., Vehkamäki, H., Petäjä, T., Dal Maso, M., Lauri, A., Kerminen, V. M., Birmili, W., and McMurry, P. H.: Formation and growth rates of ultrafine atmospheric particles: a review of observations, Aerosol Sci., 35, 143-176, 2004.

Kundu, S., Quraishi, T. A., Yu, G., Suarez, C., Keutsch, F. N., and Stone, E. A.: Evidence and quantitation

525 of aromatic organosulfates in ambient aerosols in Lahore, Pakistan, Atmos. Chem. Phys., 13, 4865-4875,
526 2013.

527 Kurtén, T., Loukonen, V., Vehkamäki, H., and Kulmala, M.: Amines are likely to enhance neutral and
528 ion-induced sulfuric acid-water nucleation in the atmosphere more effectively than ammonia, Atmos.
529 Chem. Phys., 8, 4095-4103, 2008.

530 Lee, S. H., Gordon, H., Yu, H., Lehtipalo, K., Haley, R., Li, Y., and Zhang, R.: New particle formation
531 in the atmosphere: from molecular clusters to global climate, Journal of Geophysical Research:
532 Atmospheres, 124, 7098-7146, 2019.

533 Li, D., Chen, D., Liu, F., and Wang, W.: Role of glycine on sulfuric acid-ammonia clusters formation:
534 Transporter or participator, J. Environ. Sci., 89, 125-135, 2020.

535 Li, H., Kupiainen-Määttä, O., Zhang, H., Zhang, X., and Ge, M.: A molecular-scale study on the role of
536 lactic acid in new particle formation: Influence of relative humidity and temperature, Atmos. Environ.,
537 166, 479-487, 2017.

538 Li, H., Zhong, J., Vehkamäki, H., Kurtén, T., Wang, W., Ge, M., Zhang, S., Li, Z., Zhang, X., Francisco,
539 J. S., and Zeng, X. C.: Self-catalytic reaction of SO_3 and NH_3 to produce sulfamic acid and its implication
540 to atmospheric particle formation, J. Am. Chem. Soc., 140, 11020-11028, 2018a.

541 Li, J., Tsona, N. T., and Du, L.: Effect of a single water molecule on the $HO_2 + ClO$ reaction, Phys. Chem.
542 Chem. Phys., 20, 10650-10659, 2018b.

543 Li, J., Ning, A., Liu, L., and Zhang, X.: Atmospheric bases enhanced iodic acid nucleation: altitude-
544 dependent characteristics and molecular mechanisms, Environ. Sci. Technol., 58, 16962-16973, 2024.

545 Liu, L., Yu, F., Du, L., Yang, Z., Francisco, J. S., and Zhang, X.: Rapid sulfuric acid-dimethylamine
546 nucleation enhanced by nitric acid in polluted regions, Proc. Natl. Acad. Sci. U.S.A., 118, e2108384118,
547 2021.

548 Liu, L., Zhong, J., Vehkamäki, H., Kurtén, T., Du, L., Zhang, X., Francisco, J. S., and Zeng, X. C.:
549 Unexpected quenching effect on new particle formation from the atmospheric reaction of methanol with
550 SO_3, Proc. Natl. Acad. Sci. U.S.A., 116, 24966-24971, 2019.

551 Long, B., Chang, C. R., Long, Z. W., Wang, Y. B., Tan, X. F., and Zhang, W.J.: Nitric acid catalyzed
552 hydrolysis of SO_3 in the formation of sulfuric acid: a theoretical study, Chem. Phys. Lett., 581, 26-29,
553 2013.

554 Lu, T. and Chen, F.: Multiwfn: a multifunctional wavefunction analyzer, J. Comput. Chem, 33, 580-592,
555 2012.

556 Lu, Y., Liu, L., Ning, A., Gan, Y., Liu, Y., Kurtén, T., Vehkamäki, H., and Wang, L.: Atmospheric sulfuric
557 acid-dimethylamine nucleation enhanced by trifluoroacetic acid, Geophys. Res. Lett., 47, 2020.

558 Lund, M. T., Myhre, G., and Samset, B. H.: Anthropogenic aerosol forcing under the shared
559 socioeconomic pathways, Atmos. Chem. Phys., 19, 13827-13839, 2019.

560 Luo, X. S., Tang, A. H., Shi, K., Wu, L. H., Li, W. Q., Shi, W. Q., Shi, X. K., Erisman, J. W., Zhang, F.
561 S., and Liu, X. J.: Chinese coastal seas are facing heavy atmospheric nitrogen deposition, Environ. Res.
562 Lett., 9, 2014.

563 Lv, G., Sun, X., Zhang, C., and Li, M.: Understanding the catalytic role of oxalic acid in SO3 hydration
564 to form H_2SO_4 in the atmosphere, Atmos. Chem. Phys., 19, 2833-2844, 2019.

565 Ma, F., Xie, H. B., Elm, J., Shen, J., Chen, J., and Vehkamäki, H.: Piperazine enhancing sulfuric acid-
566 based new particle formation: implications for the atmospheric fate of piperazine, Environ. Sci. Technol.,
567 53, 8785-8795, 2019.

568 Mai, T. V., Duong, M. V., Nguyen, H. T., and Huynh, L. K.: Ab initio kinetics of the $HOSO_2 + {}^3O_2$

→ SO$_3$ + HO$_2$ reaction, Phys. Chem. Chem. Phys., 20, 6677-6687, 2018.

Mochizuki, T., Kawamura, K., Miyazaki, Y., Kunwar, B., and Boreddy, S. K. R.: Distributions and sources of low-molecular-weight monocarboxylic acids in gas and particles from a deciduous broadleaf forest in northern Japan, Atmos. Chem. Phys., 19, 2421-2432, 2019.

Mochizuki, T., Kawamura, K., Nakamura, S., Kanaya, Y., and Wang, Z.: Enhanced levels of atmospheric low-molecular weight monocarboxylic acids in gas and particulates over Mt. Tai, North China, during field burning of agricultural wastes, Atmos. Environ., 171, 237-247, 2017.

Mutzel, A., Poulain, L., Berndt, T., Iinuma, Y., Rodigast, M., Böge, O., Richters, S., Spindler, G., Sipilä, M., Jokinen, T., Kulmala, M., and Herrmann, H.: Highly oxidized multifunctional organic compounds observed in tropospheric particles: a field and laboratory study, Environ. Sci. Technol., 49, 7754-7761, 2015.

Neese, F.: The ORCA program system, WIREs computational molecular science, 2, 73-78, 2012.

O'Dowd, C. D., Hämeri, K., Mäkelä, J. M., Pirjola, L., Kulmala, M., Jennings, S. G., Berresheim, H., Hansson, H. C., de Leeuw, G., Kunz, G. J., Allen, A. G., Hewitt, C. N., Jackson, A., Viisanen, Y., and Hoffmann, T.: A dedicated study of New Particle Formation and Fate in the Coastal Environment (PARFORCE): Overview of objectives and achievements, J. Geophys. Res. Atmos., 107, 2002.

Olson, C. N., Galloway, M. M., Yu, G., Hedman, C. J., Lockett, M. R., Yoon, T., Stone, E. A., Smith, L. M., and Keutsch, F. N.: Hydroxycarboxylic acid-derived organosulfates: synthesis, stability, and quantification in ambient aerosol, Environ. Sci. Technol., 45, 6468-6474, 2011.

Partanen, L., Vehkamäki, H., Hansen, K., Elm, J., Henschel, H., Kurtén, T., Halonen, R., and Zapadinsky, E.: Effect of conformers on free energies of atmospheric complexes, J. Phys. Chem. A, 120, 8613-8624, 2016.

Ristovski, Z. D., Suni, T., Kulmala, M., Boy, M., Meyer, N. K., Duplissy, J., Turnipseed, A., Morawska, L., and Baltensperger, U.: The role of sulphates and organic vapours in growth of newly formed particles in a eucalypt forest, Atmos. Chem. Phys., 10, 2919-2926, 2010.

Riva, M., Tomaz, S., Cui, T., Lin, Y.-H., Perraudin, E., Gold, A., Stone, E. A., Villenave, E., and Surratt, J. D.: Evidence for an unrecognized secondary anthropogenic source of organosulfates and sulfonates: gas-phase oxidation of polycyclic aromatic hydrocarbons in the presence of sulfate aerosol, Environ. Sci. Technol., 49, 6654-6664, 2015.

Rong, H., Liu, L., Liu, J., and Zhang, X.: Glyoxylic sulfuric anhydride from the gas-phase reaction between Glyoxylic Acid and SO$_3$: A potential nucleation precursor, J. Phys. Chem. A, 124, 3261-3268, 2020a.

Rong, H., Liu, J. R., Zhang, Y. J., Du, L., Zhang, X., and Li, Z.: Nucleation mechanisms of iodic acid in clean and polluted coastal regions, Chemosphere, 253, 126743-126752, 2020b.

Shampine, L. F. and Reichelt, M. W.: The MATLAB ode suite, SIAM journal on scientific Computing, 18, 1-22, 1997.

Shen, J., Elm, J., Xie, H. B., Chen, J., Niu, J., and Vehkamäki, H.: Structural effects of amines in enhancing methanesulfonic acid-driven new particle formation, Environ. Sci. Technol., 54, 13498-13508, 2020.

Shen, J., Xie, H.-B., Elm, J., Ma, F., Chen, J., and Vehkamäki, H.: Methanesulfonic Acid-driven new particle formation enhanced by monoethanolamine: A computational study, Environ. Sci. Technol., 53, 14387-14397, 2019.

Sipilä, M., Sarnela, N., Jokinen, T., Henschel, H., Junninen, H., Kontkanen, J., Richters, S., Kangasluoma, J., Franchin, A., Peräkylä, O., Rissanen, M. P., Ehn, M., Vehkamäki, H., Kurten, T., Berndt, T., Petäjä, T.,

Worsnop, D., Ceburnis, D., Kerminen, V.-M., Kulmala, M., and O'Dowd, C.: Molecular-scale evidence of aerosol particle formation via sequential addition of HIO_3, Nature, 537, 532-534, 2016.

Smith, C. J., Huff, A. K., Ward, R. M., and Leopold, K. R.: Carboxylic sulfuric anhydrides, J. Phys. Chem. A, 124, 601-612, 2020.

Stewart, J. J.: Optimization of parameters for semiempirical methods V: modification of NDDO approximations and application to 70 elements, J. Mol. Model., 13, 1173-1213, 2007.

Sun, H., Liu, Y., Nie, W., Li, Y., Ge, D., Xu, T., Yin, J., Liu, C., Fu, Z., Qi, X., Liu, T., Zha, Q., Yan, C., Wang, Z., Chi, X., and Ding, A.: Unexpected gas-Phase formation of Glycolic Acid Sulfate in the atmosphere, Environ. Sci. Technol., 59, 16556-16566, 2025.

Tan, S., Zhang, X., Lian, Y., Chen, X., Yin, S., Du, L., and Ge, M.: OH group orientation leads to organosulfate formation at the liquid aerosol surface, J. Am. Chem. Soc., 144, 16953-16964, 2022.

Tan, X. F., Long, B., Ren, D. S., Zhang, W. J., Long, Z. W., and Mitchell, E.: Atmospheric chemistry of CH_3CHO: the hydrolysis of CH_3CHO catalyzed by H_2SO_4, Phys. Chem. Chem. Phys., 20, 7701-7709, 2018.

Tan, X. F., Zhang, L., and Long, B.: New mechanistic pathways for the formation of organosulfates catalyzed by ammonia and carbinolamine formation catalyzed by sulfuric acid in the atmosphere, Phys. Chem. Chem. Phys., 22, 8800-8807, 2020.

Tsona Tchinda, N., Du, L., Liu, L., and Zhang, X.: Pyruvic acid, an efficient catalyst in SO_3 hydrolysis and effective clustering agent in sulfuric-acid-based new particle formation, Atmos. Chem. Phys., 22, 1951-1963, 2022.

Walker, M., Harvey, A. J. A., Sen, A., and Dessent, C. E. H.: Performance of M06, M06-2X, and M06-HF density functionals for conformationally flexible anionic clusters: M06 functionals perform better than B3LYP for a model system with dispersion and ionic hydrogen-bonding interactions, J. Phys. Chem. A., 117, 12590-12600, 2013.

Wang, R., Li, R., Chen, S., Mu, R., Zhang, C., Ma, X., Khan, M., and Zhang, T.: Enhancing SO_3 hydrolysis and nucleation: the role of formic sulfuric anhydride, Atmos. Chem. Phys., 25, 5695-5709, 2025.

Wang, Y., Hu, M., Guo, S., Wang, Y., Zheng, J., Yang, Y., Zhu, W., Tang, R., Li, X., Liu, Y., Le Breton, M., Du, Z., Shang, D., Wu, Y., Wu, Z., Song, Y., Lou, S., Hallquist, M., and Yu, J.: The secondary formation of organosulfates under interactions between biogenic emissions and anthropogenic pollutants in summer in Beijing, Atmos. Chem. Phys., 18, 10693-10713, 2018.

Wang, Z. B., Hu, M., Yue, D. L., Zheng, J., Zhang, R. Y., Wiedensohler, A., Wu, Z. J., Nieminen, T., and Boy, M.: Evaluation on the role of sulfuric acid in the mechanisms of new particle formation for Beijing case, Atmos. Chem. Phys., 11, 12663-12671, 2011.

Wardlaw, D. M. and Marcus, R. A.: RRKM reaction rate theory for transition states of any looseness, Chem. Phys. Lett., 110, 230-234, 1984.

Wu, S., Dai, L. H., Wei, Y., Zhu, H., Zhang, Y. J., Schwab, J., and Yuan, C. S.: Atmospheric ammonia measurements along the coastal lines of Southeastern China: Implications for inorganic nitrogen deposition to coastal waters, Atmos. Environ., 177, 1-11, 2017.

Xing, Y. F., Xu, Y. H., Shi, M. H., and Lian, Y. X.: The impact of PM2.5 on the human respiratory system, J. Thorac. Dis., 8, 69-74, 2016.

Yang, Y., Liu, L., Wang, H., and Zhang, X.: Molecular-scale mechanism of sequential reaction of oxalic acid with SO_3: potential participator in atmospheric aerosol nucleation, J. Phys. Chem. A, 125, 4200-4208, 2021.

Yao, L., Garmash, O., Bianchi, F., Zheng, J., Yan, C., Kontkanen, J., Junninen, H., Mazon, S. B., Ehn, M., Paasonen, P., Sipilä, M., Wang, M., Wang, X., Xiao, S., Chen, H., Lu, Y., Zhang, B., Wang, D., Fu, Q., Geng, F., Li, L., Wang, H., Qiao, L., Yang, X., Chen, J., Kerminen, V. M., Petäjä, T., Worsnop, D. R., Kulmala, M., and Wang, L.: Atmospheric new particle formation from sulfuric acid and amines in a Chinese megacity, Science, 361, 278-281, 2018.

Yao, L., Fan, X., Yan, C., Kurtén, T., Daellenbach, K. R., Li, C., Wang, Y., Guo, Y., Dada, L., Rissanen, M. P., Cai, J., Tham, Y. J., Zha, Q., Zhang, S., Du, W., Yu, M., Zheng, F., Zhou, Y., Kontkanen, J., Chan, T., Shen, J., Kujansuu, J. T., Kangasluoma, J., Jiang, J., Wang, L., Worsnop, D. R., Petäjä, T., Kerminen, V. M., Liu, Y., Chu, B., He, H., Kulmala, M., and Bianchi, F.: Unprecedented ambient sulfur trioxide (SO$_3$) detection: possible formation mechanism and atmospheric implications, Environ. Sci. Technol., 7, 809-818, 2020.

Yin, R., Yan, C., Cai, R., Li, X., Shen, J., Lu, Y., Schobesberger, S., Fu, Y., Deng, C., Wang, L., Liu, Y., Zheng, J., Xie, H., Bianchi, F., Worsnop, D. R., Kulmala, M., and Jiang, J.: Acid-base clusters during atmospheric new particle formation in urban Beijing, Environ. Sci. Technol., 55, 10994-11005, 2021.

Zhang, H., Kupiainen-Määttä, O., Molinero, V., Zhang, Y., and Li, Z.: The enhancement mechanism of glycolic acid on the formation of atmospheric sulfuric acid-ammonia molecular clusters, J. Chem. Phys., 146, 184308, 2017.

Zhang, H., Gao, R., Li, H., Li, Y., Xu, Y., and Chai, F.: Formation mechanism of typical aromatic sulfuric anhydrides and their potential role in atmospheric nucleation process, J. Environ. Sci., 123, 54-64, 2023a.

Zhang, H., Li, H., Liu, L., Zhang, Y., Zhang, X., and Li, Z.: The potential role of malonic acid in the atmospheric sulfuric acid-ammonia clusters formation, Chemosphere, 203, 26-33, 2018.

Zhang, H., Wang, W., Fan, L., Li, J., Ren, Y., Li, H., Gao, R., and Xu, Y.: The role of sulfur cycle in new particle formation: Cycloaddition reaction of SO$_3$ to H$_2$S, J. Environ. Sci., 148, 489-501, 2025.

Zhang, H., Worton, D. R., Lewandowski, M., Ortega, J., Rubitschun, C. L., Park, J.-H., Kristensen, K., Campuzano-Jost, P., Day, D. A., Jimenez, J. L., Jaoui, M., Offenberg, J. H., Kleindienst, T. E., Gilman, J., Kuster, W. C., de Gouw, J., Park, C., Schade, G. W., Frossard, A. A., Russell, L., Kaser, L., Jud, W., Hansel, A., Cappellin, L., Karl, T., Glasius, M., Guenther, A., Goldstein, A. H., Seinfeld, J. H., Gold, A., Kamens, R. M., and Surratt, J. D.: Organosulfates as tracers for secondary organic aerosol (SOA) formation from 2-Methyl-3-Buten-2-ol (MBO) in the atmosphere, Environ. Sci. Technol., 46, 9437-9446, 2012a.

Zhang, J. and Dolg, M.: Global optimization of clusters of rigid molecules using the artificial bee colony algorithm, Phys. Chem. Chem. Phys., 18, 3003-3010, 2016.

Zhang, Q., Wang, Y., Liu, M., Zheng, M., Yuan, L., Liu, J., Tao, S., and Wang, X.: Wintertime formation of large sulfate particles in China and implications for human health, Environ. Sci. Technol., 57, 20010-20023, 2023b.

Zhang, R., Khalizov, A., Wang, L., Hu, M., and Xu, W.: Nucleation and growth of nanoparticles in the atmosphere, Chem. Rev., 112, 1957-2011, 2012b.

Zhang, R., Wang, G., Guo, S., Zamora, M. L., Ying, Q., Lin, Y., Wang, W., Hu, M., and Wang, Y.: Formation of urban fine particulate matter, Chem. Rev., 115, 3803-3855, 2015.

Zhang, X. M., Lian, Y. J., Tan, S. D., and Yin, S.: Organosulfate produced from consumption of SO$_3$ speeds up sulfuric acid-dimethylamine atmospheric nucleation, Atmos. Chem. Phys., 24, 3593-3612, 2024.

Zhao, B., Donahue, N. M., Zhang, K., Mao, L., Shrivastava, M., Ma, P.-L., Shen, J., Wang, S., Sun, J., Gordon, H., Tang, S., Fast, J., Wang, M., Gao, Y., Yan, C., Singh, B., Li, Z., Huang, L., Lou, S., Lin, G.,

701 Wang, H., Jiang, J., Ding, A., Nie, W., Qi, X., Chi, X., and Wang, L.: Global variability in atmospheric
702 new particle formation mechanisms, Nature, 631, 98-105, 2024.
703 Zheng, B., Tong, D., Li, M., Liu, F., Hong, C., Geng, G., Li, H., Li, X., Peng, L., Qi, J., Yan, L., Zhang,
704 Y., Zhao, H., Zheng, Y., He, K., and Zhang, Q.: Trends in China's anthropogenic emissions since 2010 as
705 the consequence of clean air actions, Atmos. Chem. Phys., 18, 14095-14111, 2018.
706 Zu, H., Zhang, S., and Liu, L.: The vital role of sulfuric acid in iodine oxoacids nucleation: impacts of
707 urban pollutants on marine atmosphere, Environ. Res. Lett., 19, 2024a.
708 Zu, H., Zhang, S., Li, S., Liu, L., and Zhang, X.: The synergistic nucleation of iodous acid and sulfuric
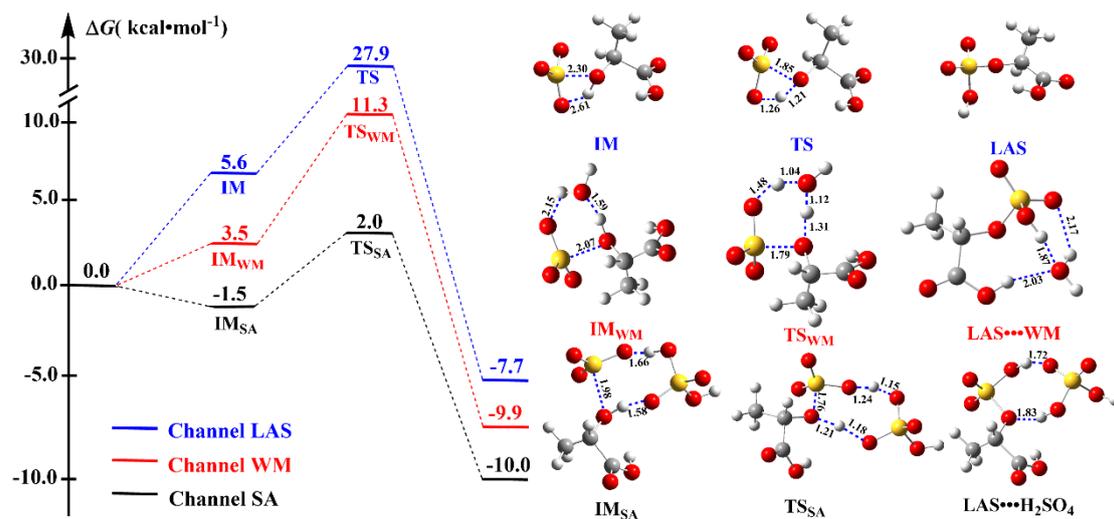709 acid: A vital mechanism in polluted marine regions, Atmos. Environ., 318, 120266, 2024b.
710

711
712
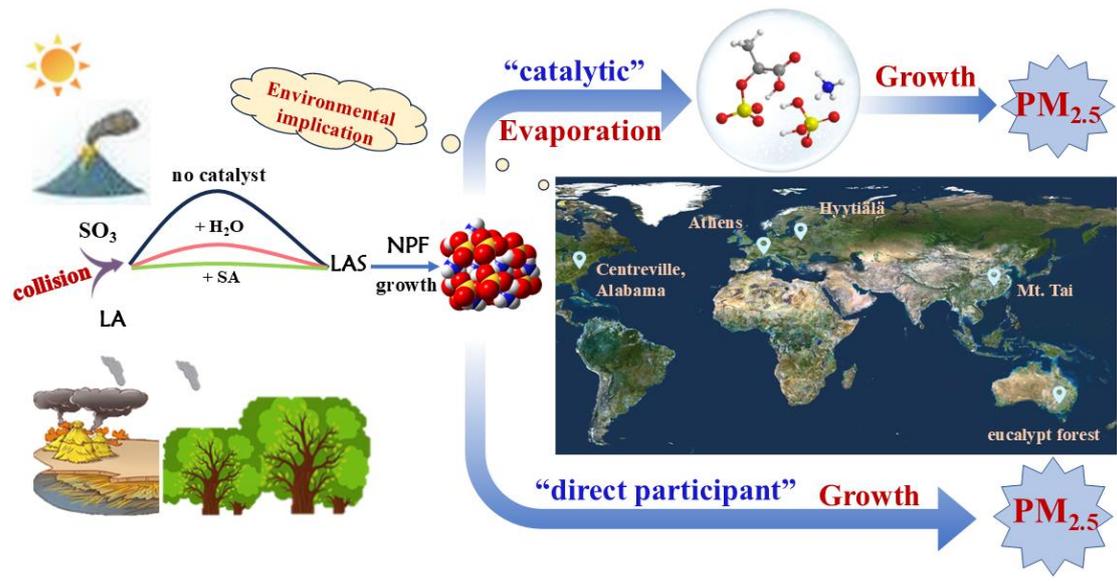
713 **Graphic abstract**

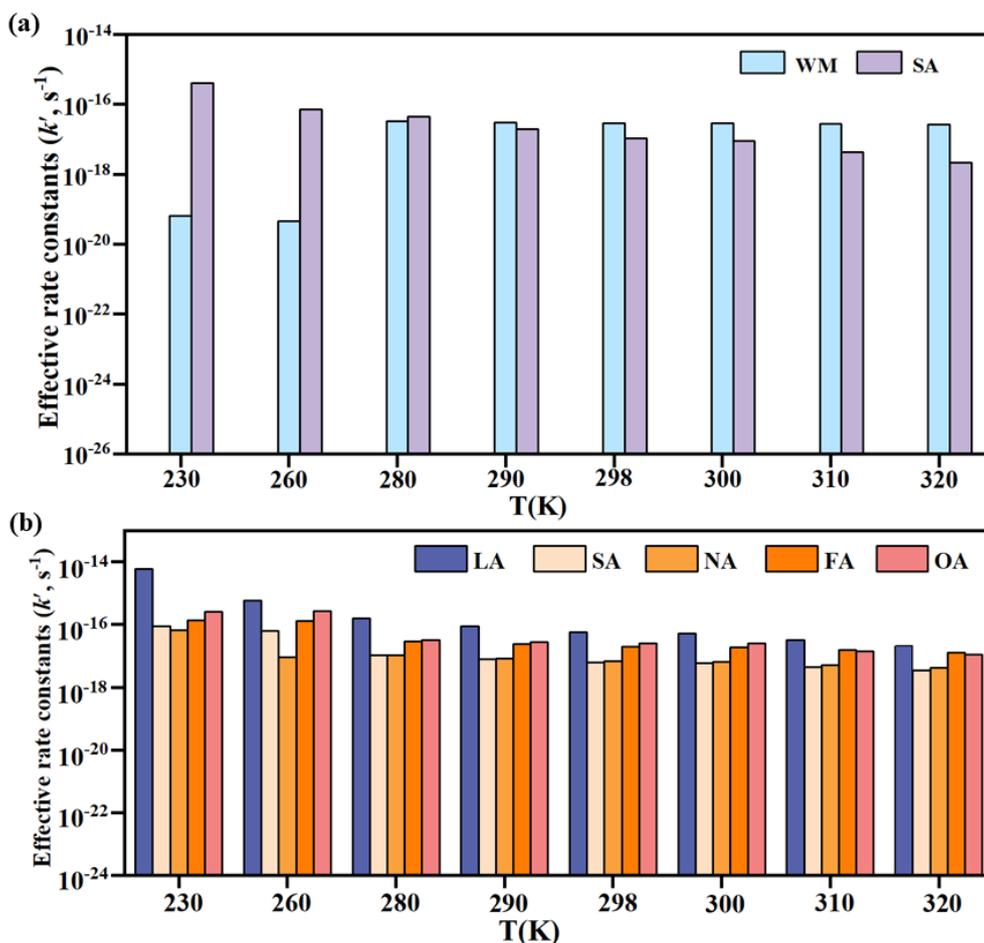**Fig. 1** Potential energy profiles and corresponding molecular structures for the LA + SO_3 → LAS reaction in the absence and presence of H_2O and H_2SO_4 investigated at the CCSD(T)-F12/cc-pVDZ-F12//M06-2X/6-311++G(2*df*,2*pd*) level

718

719 **Fig. 2** (a) Effective rate constants for the LA + SO$_3$ → LAS reaction in the presence of H$_2$O (k'_{WM},

720 cm^3·molecule^{-1}·s^{-1}) and H$_2$SO$_4$ (k'_{SA}, cm^3·molecule^{-1}·s^{-1}) calculated using the master equation over

721 the temperature range of 230-320 K; (b) Effective rate constants (k', s^{-1}) for the hydrolysis of SO$_3$

722 with various species X (X = LA, SA , NA, FA and OA) within the temperature range of 230-320 K,

723 where SA , NA, FA and OA are denoted as H$_2$SO$_4$, HNO$_3$, HCOOH and H$_2$C$_2$O$_4$, respectively.

724
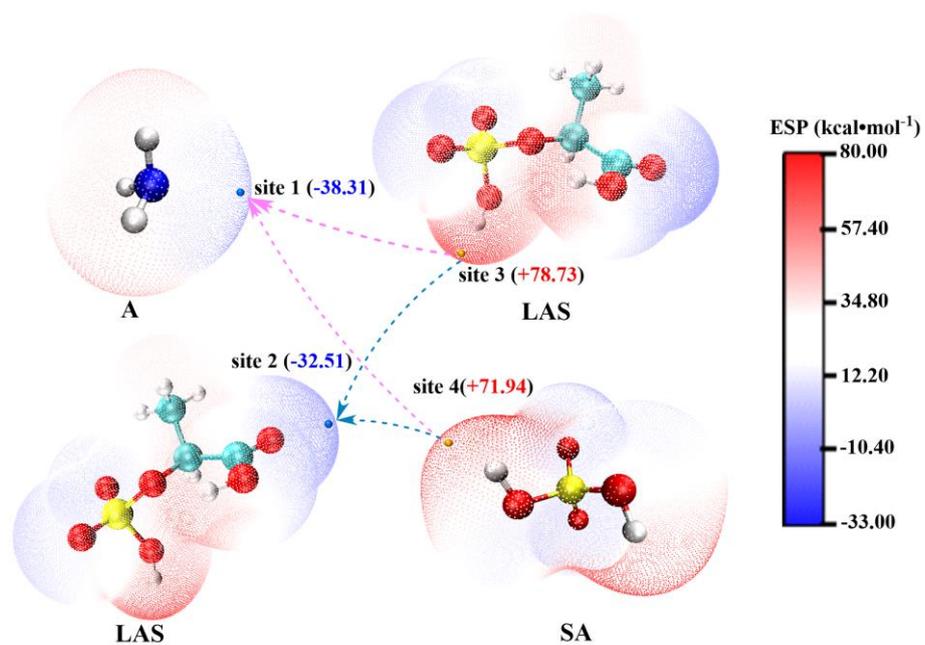
725

726 **Fig. 3** Electrostatic potential (ESP)-mapped van der Waals surfaces of A, LAS and SA molecules.
727 ESP minima and maxima for different functional groups are shown as blue and yellow spheres,
728 respectively, with their corresponding values (kcal·mol^{-1}) indicated in parentheses. Red arrows
729 denote preferred directions for hydrogen bond formation, while blue arrows illustrate likely
730 pathways for proton transfer.
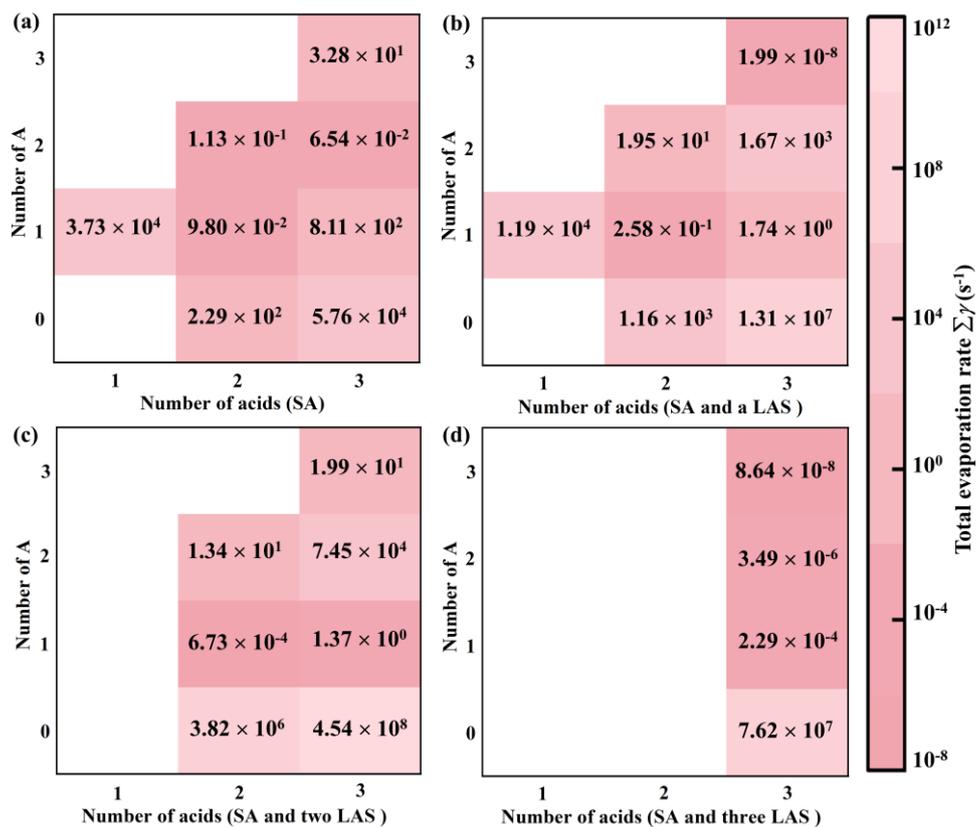
731
732 **Fig. 4** The total evaporation rates ($\sum\gamma$) (s^{-1}) of $(SA)_x(A)_y(LAS)_z$ ($y \leq x + z \leq 3$) clusters at 278.15 K
733 and 1 atm calculated at the M06-2X/6-311++G($2df$, $2pd$) level of theory. (a) without LAS monomer,
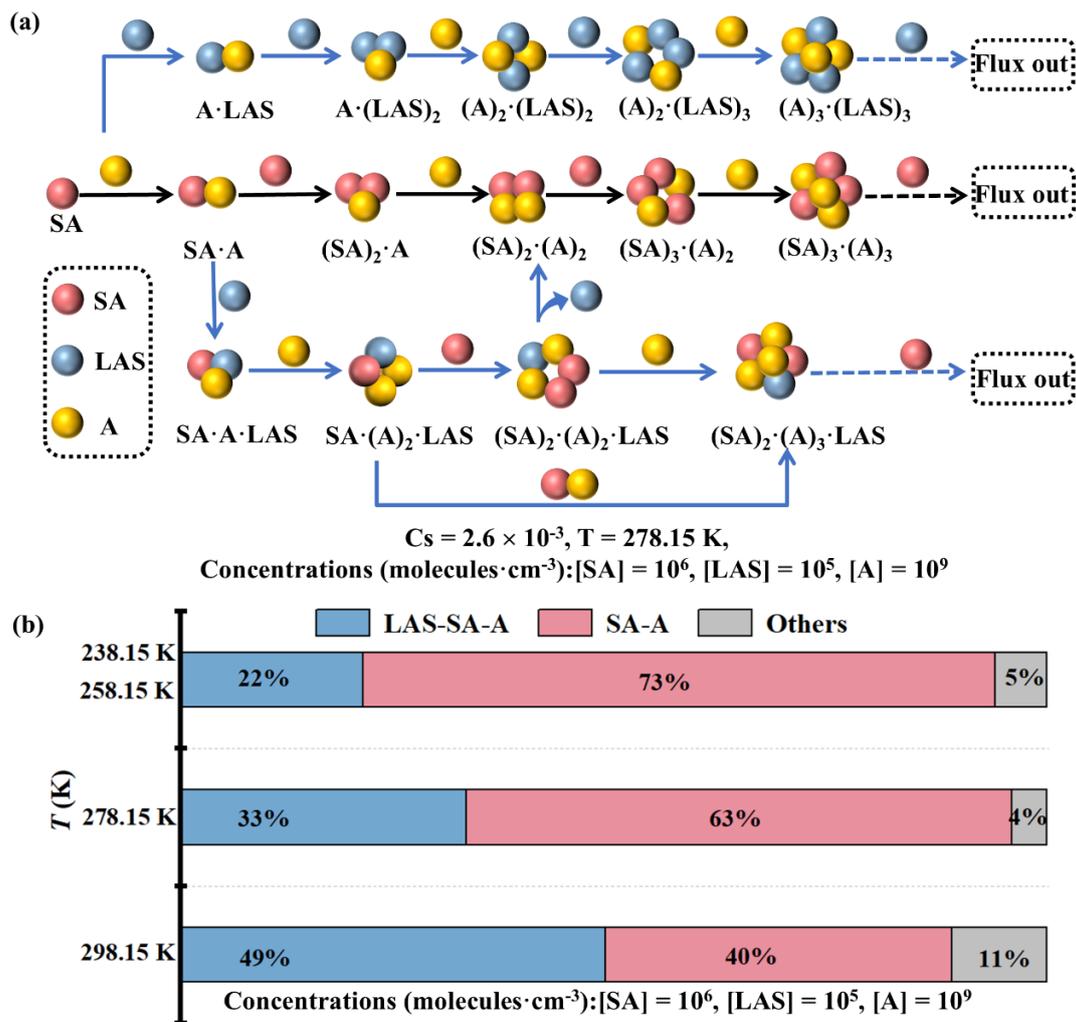734 (b) containing 1 LAS monomer, (c) containing 2 LAS monomers, and (d) containing 3 LAS
735 monomers

(a)

A·LAS   A·(LAS)$_2$ (A)$_2$·(LAS)$_2$ (A)$_2$·(LAS)$_3$ (A)$_3$·(LAS)$_3$ Flux out

SA   SA·A   (SA)$_2$·A   (SA)$_2$·(A)$_2$ (SA)$_3$·(A)$_2$ (SA)$_3$·(A)$_3$ Flux out

SA   LAS   A

SA·A·LAS   SA·(A)$_2$·LAS   (SA)$_2$·(A)$_2$·LAS   (SA)$_2$·(A)$_3$·LAS   Flux out

$Cs = 2.6 \times 10^{-3}$, $T = 278.15$ K,
Concentrations (molecules·cm^{-3}):[SA] = 10^6, [LAS] = 10^5, [A] = 10^9

(b)

LAS-SA-A   SA-A   Others

238.15 K / 258.15 K: 22%   73%   5%

278.15 K: 33%   63%   4%

298.15 K: 49%   40%   11%

T (K)

Concentrations (molecules·cm^{-3}):[SA] = 10^6, [LAS] = 10^5, [A] = 10^9
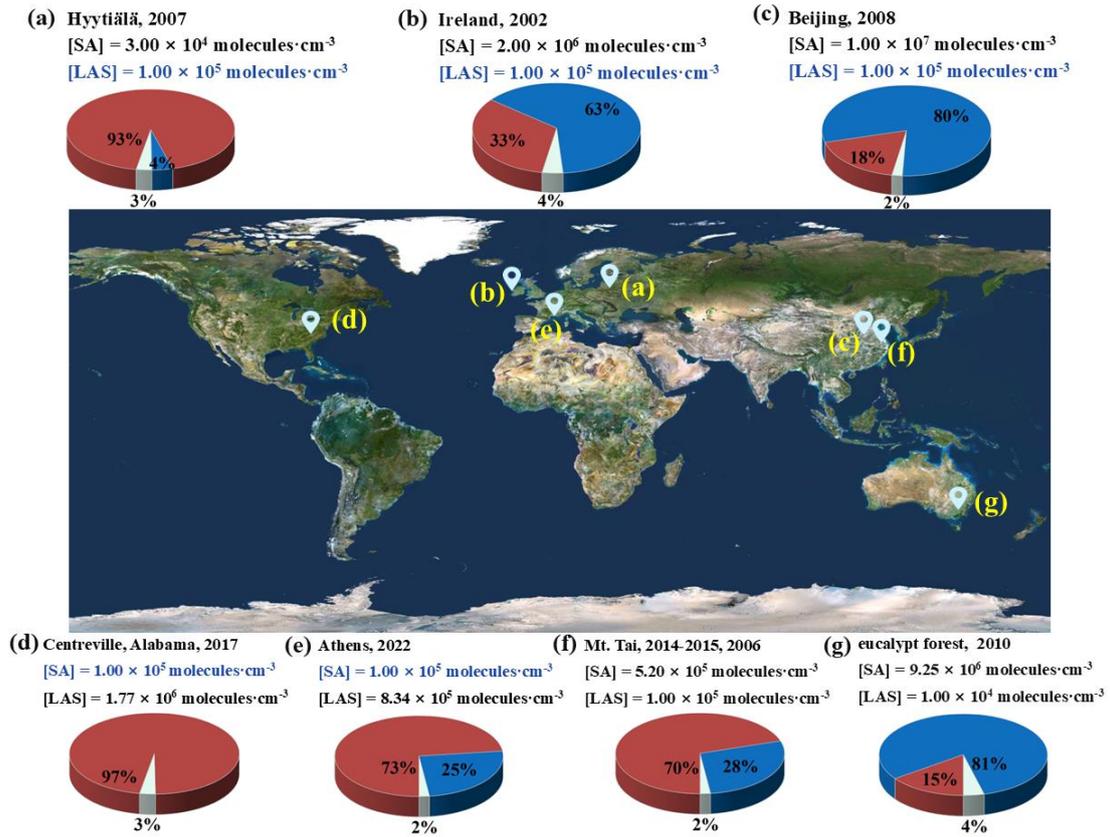
Fig. 5 Nucleation mechanism of the LAS-SA-A system. (a) Cluster formation pathway at 278.15 K, with concentrations of [SA] = 10^6, [A] = 10^9 and [LAS] = 10^5 molecules·cm^{-3}; (b) the branch ratio of outward flux at different temperatures. Only net fluxes contributing more than 5% to cluster growth are depicted.

(a) Hyytiälä, 2007
[SA] = 3.00×10^4 molecules·cm^{-3}
[LAS] = 1.00×10^5 molecules·cm^{-3}

(b) Ireland, 2002
[SA] = 2.00×10^6 molecules·cm^{-3}
[LAS] = 1.00×10^5 molecules·cm^{-3}

(c) Beijing, 2008
[SA] = 1.00×10^7 molecules·cm^{-3}
[LAS] = 1.00×10^5 molecules·cm^{-3}

(d) Centreville, Alabama, 2017
[SA] = 1.00×10^5 molecules·cm^{-3}
[LAS] = 1.77×10^6 molecules·cm^{-3}

(e) Athens, 2022
[SA] = 1.00×10^5 molecules·cm^{-3}
[LAS] = 8.34×10^5 molecules·cm^{-3}

(f) Mt. Tai, 2014-2015, 2006
[SA] = 5.20×10^5 molecules·cm^{-3}
[LAS] = 1.00×10^5 molecules·cm^{-3}

(g) eucalypt forest, 2010
[SA] = 9.25×10^6 molecules·cm^{-3}
[LAS] = 1.00×10^4 molecules·cm^{-3}

Fig. 6 Branching ratios of SA-A-LAS (red) and SA-A (blue) cluster growth pathways in regions with varying [LAS] concentrations. Black data points indicate field observations, while blue points represent the median values used in this study. Ammonia concentration is fixed at 10^9 molecules·cm^{-3}. Map source: ©Google Maps (https://www.google.com/maps)
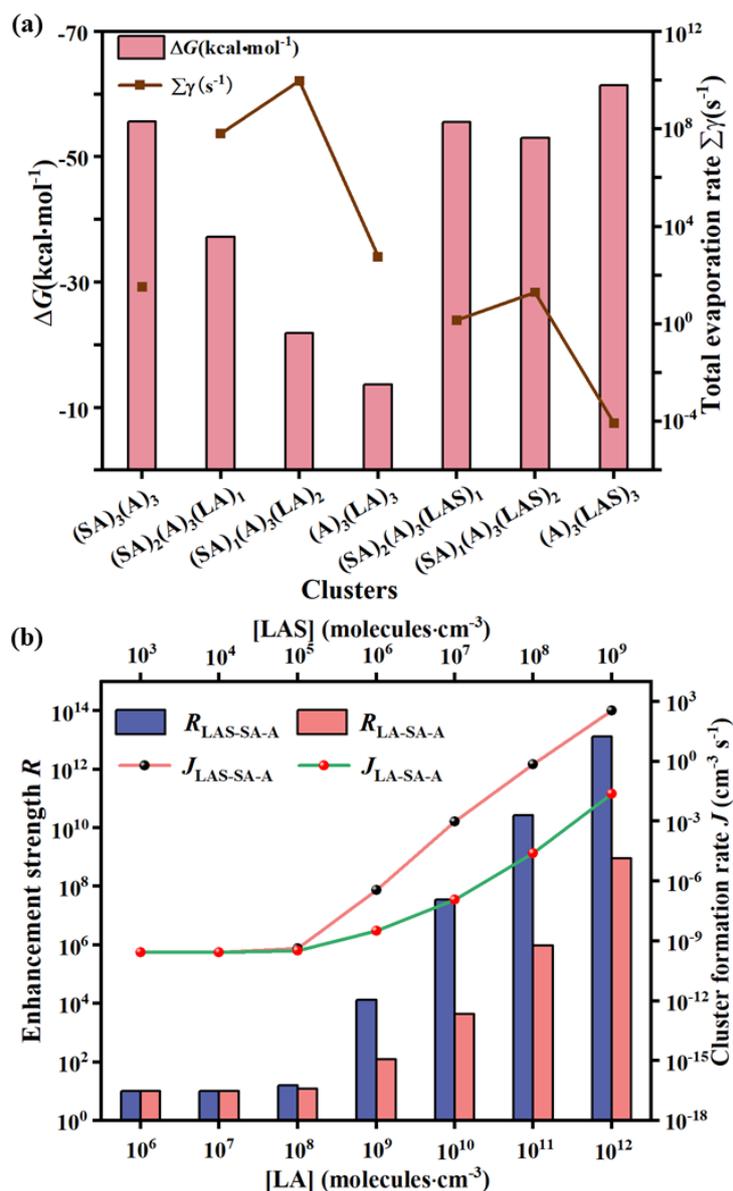
Fig. 7 (a) Gibbs free energies ΔG (kcal·mol^{-1}) and total evaporation rates $\sum \gamma$ (s^{-1}) for (LA)$_x$(SA)$_y$(A)$_3$ and (LAS)$_x$(SA)$_y$(A)$_3$ (x = 0-3, $x + y$ = 3) clusters calculated at the M06-2X/6-311++G(2df, 2pd) level of theory and 278.15 K; (b) Cluster formation rate (J) and enhancement strength (R) for LAS as a function of monomer concentrations ([LA] and [LAS]) at 278.15 K, with [SA] fixed at 10^5 molecules·cm^{-3} and [A] at 10^9 molecules·cm^{-3}.